Modulating the properties of multifunctional semiconductors by means of morphology: Theory meets experiments

Amanda F. Gouveia[a,b], Lourdes Gracia[a(1)], Elson Longo[c], Miguel A. San-Miguel[b], Juan Andrés[a]

[a]*Department of Physical and Analytical Chemistry, Universitat Jaume I (UJI), 12071 Castelló, Spain.*

[b]*Institute of Chemistry, State University of Campinas (Unicamp), 13083-970 Campinas, SP, Brazil.*

[c]*CDMF, Federal University of São Carlos (UFSCar), P.O. Box 676, 13565-905, São Carlos, SP, Brazil.*

[(1)]*Permanent address: Department of Physical Chemistry, Universitat de Valencia (UV), 46100 Burjassot, Spain.*

ABSTRACT

Morphology control of multifunctional semiconductor materials is a significant topic since it directly impacts the physical and chemical properties in catalysis, photonics, energy conversion, and other applications. Therefore, the characterization and the control of the morphology of (nano)materials is of fundamental importance in materials science and nanotechnology. Deep insights into the chemical nature of surface energy, composition, structure, and electronic properties of the exposed surfaces that constitute the crystal morphology are important to achieve a rational design of solid materials with desired morphologies and functionalities such as electronic properties and catalytic performances and biocide activity. The morphologies are determined by the values of surface energies of different families of crystal planes, calculated by density functional theory and Wulff construction by a 'brute-force' method. As part of the special issue on Rising Stars in Computational Materials Science, this work presents computational studies coupled with field emission scanning electron microscopy images that reflect their utility as an effective method for exploring a vast array of morphologies, allowing for a rigorous investigation of surface structures. We have demonstrated that the simulated morphologies from present models match the experimental results quite well. Based on this good agreement in terms of geometric structure and relative stability between, we propose a new concept to describe the atomic coordination environment of surface atoms, to find a relationship between the material properties (photocatalytic and biocide activities) and the exposed surface at the morphology, as well as to present reasons for the generation of reactive oxygen species in the α-Ag_2WO_4 and β-Ag_2MoO_4 materials. This strategy offers not only a rationalization and explanation of the behaviors and properties of the materials but also can be used to explain the corresponding action mechanism.

KEYWORDS: Morphology, Exposed surfaces, Wulff construction, DFT calculations, Photocatalytic activity, Biocide activity.

1. Introduction

The anisotropy of single crystals provides a platform for many interesting applications along different crystallographic directions. Both crystal and surface structures of a semiconductor are perhaps the most important parameters that dictate its physicochemical properties and related applications. Crystal structures define its electronic properties by means of the stacking sequence of atoms, ions, or molecules, following the symmetry group of a crystalline material, while surfaces play a central role in many multifunctional semiconductors because their main properties are controlled by the morphology through adjusting atomic configurations at the exposed surfaces [1-7].

The morphology not only determines the stability of the entire system, but also defines the local atomic arrangements that strongly influence the chemical reactivity. Therefore, morphology has an impact on the performance of materials in a wide range of applications and can be associated directly with surface structures and states (defects, surface atom density, surface atom arrangement, and so on) [8-14]. It is not surprising that during research on the surface properties, an interesting but also troublesome phenomenon drawing many researchers' attention is that the surface properties of solids at different crystal surfaces demonstrate distinctive differences, being the focus of many fields such as catalysis, and micro- or nano-scale surface materials [15-18]. Consequently, the understanding of the electronic structure of semiconductors is key; not only to optimizing and fine-tuning their performance but also to aiding the design of novel materials with tailored properties. In this context, morphology-controlled inorganic semiconductors have attracted a huge amount of attention owing to both their unique material properties, and their consequent theoretical and practical applications in chemistry, physics, materials science, biology, and medicine [19-24].

The aims of this perspective review are the following: (1) to circulate current knowledge of the morphology of materials, (2) to summarize state-of-the-art developments in their experimental and theoretical aspects, and (3) to discuss current theoretical and computational approaches and their relationship to photocatalytic and biocide activities for a wide spectrum of scientists including graduate students.

2. State-of-the-art morphology and properties

Diverse semiconductors can be found in various areas of science and technology, due to their marvelous morphology-dependent physical and chemical properties [25-35]. In this context, surface structures play an important role because the photocatalytic reaction or photoelectron conversion only takes place when photoinduced electrons (e^-) and holes (h^+) are available on the surface. However, the geometry and crystal structures become more complicated at a surface or interface compared to the bulk material. From an experimental perspective, molecular adsorption and interfacial bonding take place in the surface layers, which require challenging interface-specific spectroscopies to accurately characterize. In addition, from a theoretical point of view, surfaces lack the periodicity of bulk crystals, making them challenging to calculate.

The knowledge and the understanding of how a given crystal morphology is achieved constitutes a rich information to the experimentalists. This is the basis to a rational synthesis design to control the stability of a given exposed surface to end up in the desired morphology. At this point, it is important to recognize that adjusting morphologies and surface structures of crystals are, however, highly sensitive to the experimental conditions, such as method of synthesis, type of solvent, presence of surfactants, time of processing, temperature, pressure,

3

and pH; thus complicating photocatalyst optimization. These variables are responsible for the stabilization or destabilization of the exposed surfaces resulting in different morphologies.

Along the synthesis, crystal growth is a continuous process involving reactant ions, centered at their corresponding clusters, i.e. the local coordination of cations with oxygen cations in metal oxides. These clusters display positive and negative charges, and this imbalance provokes electron transfer among them, which perform effective and non-effective random shocks. In this way, these clusters, as building blocks of the material and fixed after nucleation, yield not only the structure in the short, medium and the bulk long-range order that determines the crystalline structure, but also the final morphology.

Changes in the material morphology affect the corresponding properties and then the low or high response of certain applications. The efficiency of the materials depends on the surface composition involving the active sites, i.e., the undercoordinated clusters, in turn, are related to the morphologies, as schematically illustrated in **Fig. 1**. Cutting the right exposed surfaces of crystals is challenging because the native cleavage planes of crystals are definite. Therefore, there is a clear need for systematic ways to search for the potential material design space, to narrow down the focus on materials that are expected to be high-performing.
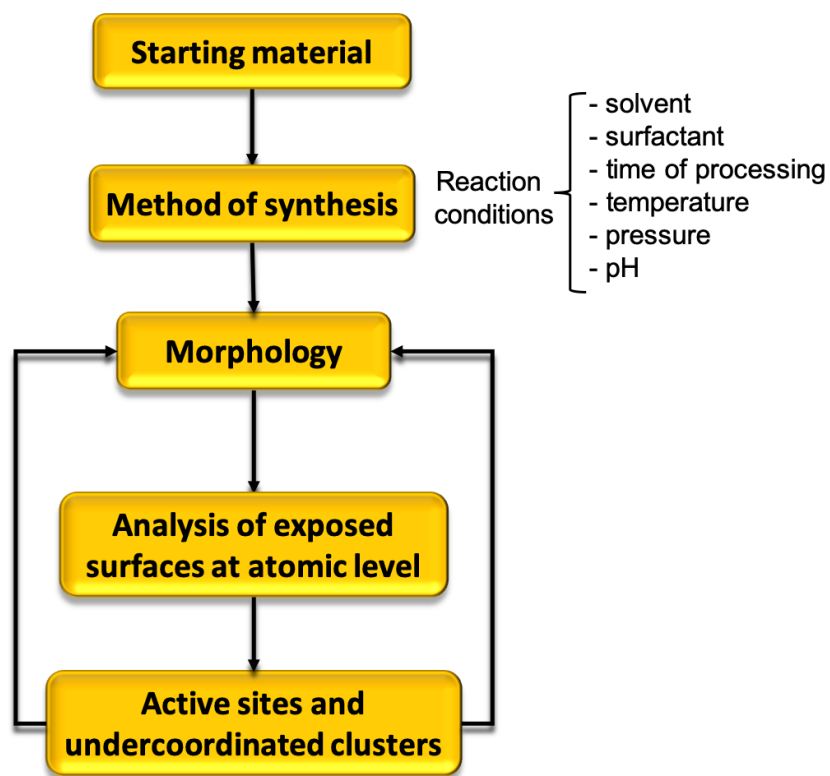
Fig. 1. A schematic representation to connect the starting material via method of synthesis, morphology, active sites and undercoordinated clusters of the exposed surfaces.

It is necessary to understand the nature and effect of the distinct active sites at the morphology of semiconductors, i.e. the undercoordinated atomic positions at the exposed surfaces, to directly relate structure and function. Therefore, it is important to construct quantitative models to purposely design new materials with new properties and applicability through controlling their morphology. The possibility of manipulating parameters gives way to modeling and simulation methods, modeling at the atomic level, certain advantages to study and understand complex systems over experimental techniques. In recent decades, results derived from first-principles calculations are able to reveal fundamental to capture not only the geometric and electronic effects on the properties of materials but also to explain and rationalize the experimental data.

2.1. Wulff construction

It is generally accepted that the morphology of crystals at equilibrium or quasi-equilibrium conditions is determined by the surface's thermodynamics. The surface energy (γ_{surf}) of a single-element solid is dependent on temperature, vapor pressure, and surface relaxations or reconstructions. But, in fact, measuring γ_{surf} is generally a difficult task even for simple cases [36-40]. The structure and morphology of crystals are determined by the γ_{surf} of planes on the condition of thermodynamic equilibrium, where the rate of each individual surface change is dependent on the different values of γ_{surf} [41-44].

Wulff construction, based on the minimization of the energy associated with all surrounding surfaces of an independent particle, is a reliable tool to understand and predict (nano)particle morphology [36, 43, 45-48]. According to the theory, the structure and morphology of crystals are determined by the γ_{surf} of planes on the condition of thermodynamic equilibrium [37]. Wulff construction relates the polar plot of a given material's anisotropic γ_{surf}, which is the morphology with the lowest γ_{surf} for a given volume. These γ_{surf} values, obtained by first-principles calculations in association with the Wulff construction model provide a strong correlation between structure-function, based on atomistic modeling in morphological analysis, highlighting the importance of theoretical chemistry in science materials and nanotechnology. Other thermodynamic models may also require γ_{surf} of materials as input parameters. As for thermodynamic morphology models beyond the Wulff construction, Barnard and coauthors [49, 50] developed a general thermodynamic model that includes γ_{surf}, surface stresses, hydraulic pressures, corner energies, and edge energies, while Müller and Mottet [51] also pointed out that energies of a particle's core, surfaces, edges, and corners should be included in the minimization of the total energy of the particle.

2.2. How to access the map of available morphologies

First-principles calculations based on density functional theory (DFT) has become an effective tool to calculate the γ_{surf}. By combining the values of γ_{surf} and Wulff construction the crystal morphologies of materials with well-defined crystal compositions and structures are obtained. **Fig. 2** displays the steps involved in the DFT calculations.
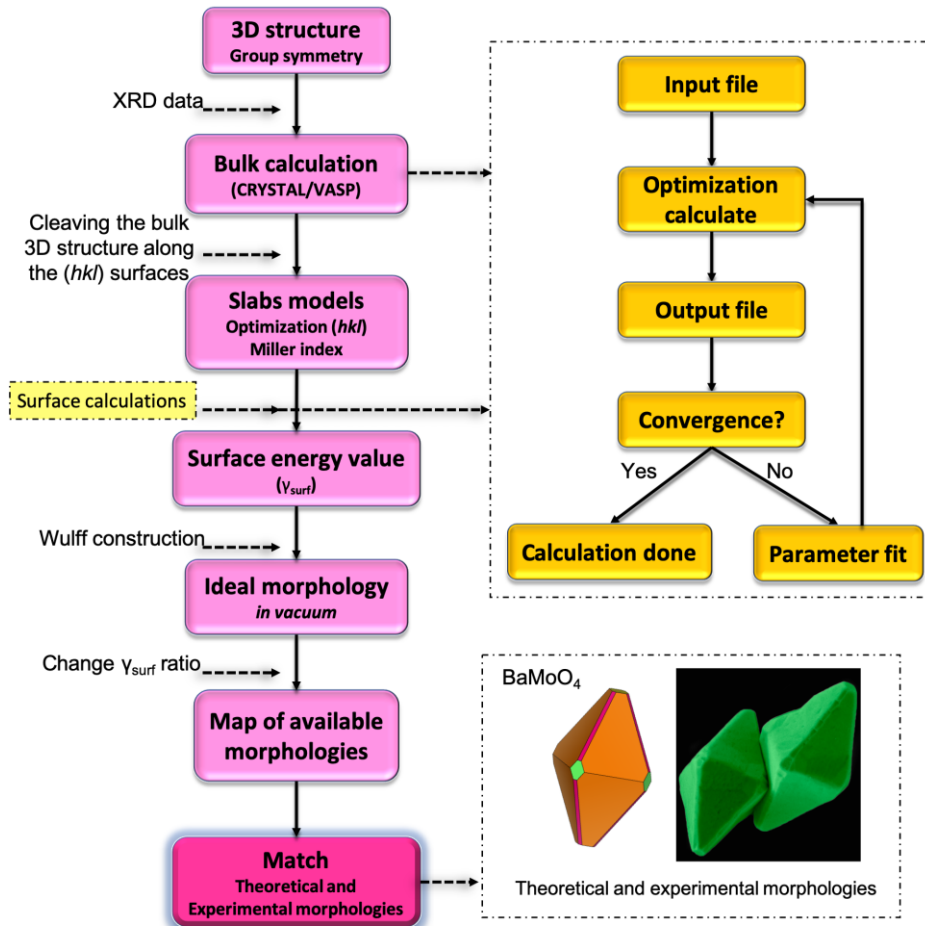
Fig. 2. High-throughput workflow for surface calculations to achieve the match between the theoretical and experimental morphologies. The case of BaMoO₄ has been selected for comparison purposes.

The first step of the workflow is the construction of the bulk structure from the X-ray diffraction (XRD) data, based on the symmetry group of 3D structure, followed by the optimization process. The next step is the construction of the slab models that starts from the optimized theoretical parameters for the unit cell of the material (bulk parameters). The Miller index associated to the cleaved surfaces are simulated.

To accurately evaluate the formation energies of different crystal surfaces, the typical slab model was used in the calculations. This model is constructed by selectively exposing the plane of interest and removing a portion of atoms to form a *vacuum*. All slab models are constrained to the symmetrical top and bottom surfaces. The values of γ_{surf} can be calculated by the equation (1):

$$\gamma_{surf} = \frac{\left[E_{slab} - \left(\frac{N_{slab}}{N_{bulk}}\right)E_{bulk}\right]}{2A} \qquad (1)$$

where the E_{slab} and the E_{bulk} are the total energies of the surface slab model and the bulk (unit cell) respectively; N refers to the number of atoms in the slab (N_{slab}) and in the bulk (N_{bulk}); 2A is the area of both sides in z-axis of the slab. Both bulk and slab surface models were optimized after the corresponding converge tests by using DFT calculations.

It is important to note that equation (1) considers symmetric and stoichiometric termination. To study symmetric/non-stoichiometric, asymmetric/stoichiometric, and asymmetric/non-stoichiometric terminations, some improvements have been considered in the literature [52]. Therefore, further analysis was performed to validate our method and the next stage is access to the available morphologies, as introduced in the paper entitled "Effects of surface stability on the morphological transformation of metals and metal oxides as investigated by first-principles calculations" published in Nanotechnology [53]. We proposed a new methodology based on the combination of the calculated values of γ_{surf} and the Wulff construction to obtain a set of available morphologies for the crystals, i.e., not only the ideal morphology *in vacuum*, but also a map of possible morphologies for a given material, demonstrating that the structural transformations among different morphologies were easily controlled by the relative values of γ_{surf}.

The development of this new approach allows the computational exploration of surface structures and morphologies. Their intrinsic properties in tandem with advances in electron microscopy techniques have resulted in its increased attention in a variety of fields, the map of

morphology being a powerful tool for the experimentalist during the field emission scanning electron microscopy (FE-SEM) analysis.

Disentangling the changes of morphology proves to be intricate due to the dynamic nature of, i.e. structure, composition and oxidation state, etc. becoming altered during the synthetic process. The results of the morphology obtained in the different synthesis methods are analyzed in FE-SEM in light of theoretical probabilities. This opens the door to a new interpretation and rationalization of the images obtained by electron microscopy, and it is a reliable tool to confront theoretical-experimental deductions.

This method was used not only to rationalize the surface structures, which has already been identified as an important phenomenon in surface stability, but also to match the theoretical to the experimental morphology. The crystal morphologies are formed by a set of surfaces with different Miller indices and can be investigated by the images obtained in the FE-SEM analysis. The high-resolution images from FE-SEM analysis could be analyzed to match with the theoretical morphologies displayed in the map.

By modulating the values of γ_{surf}, as shown in **Fig. 3**, the available morphologies are obtained. For comparison purposes, some experimental FE-SEM images of different materials are included. The ratio values between the γ_{surf} to obtain some available morphologies for a cubic structure are shown in **Table 1**.
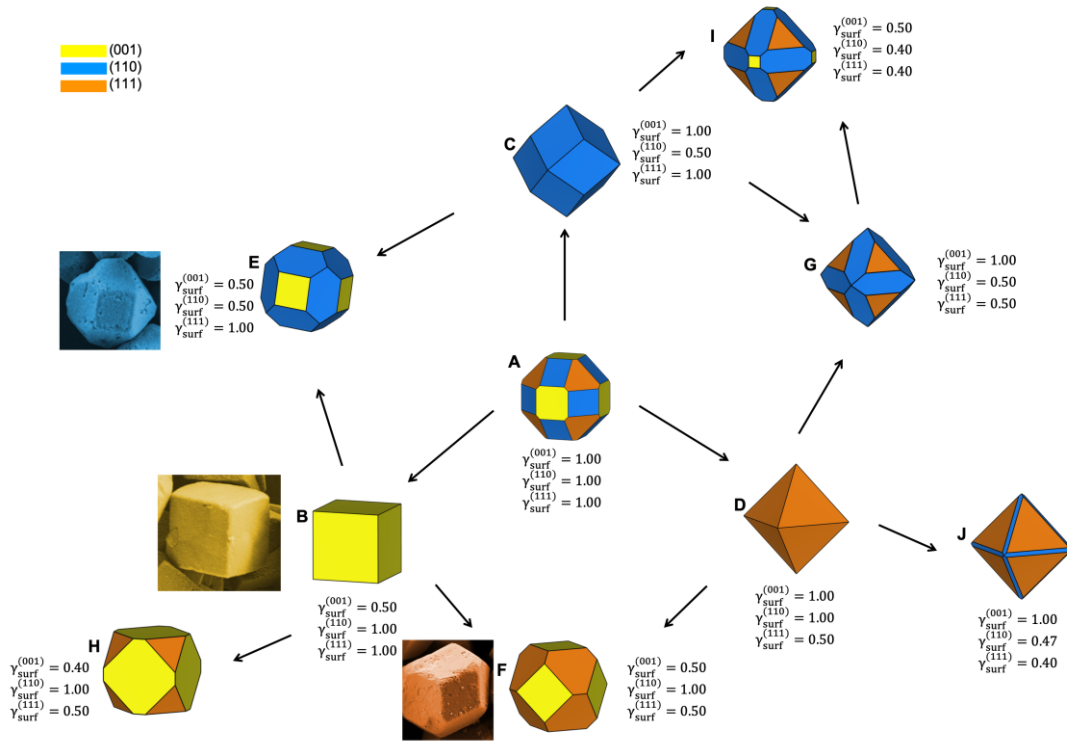
Fig. 3. Available morphologies for a cubic structure. The FE-SEM images from the β-Ag$_2$MoO$_4$ have been selected for comparison purposes. The γ$_{surf}$ values are in J/m^2.

Table 1. Ratio values between the γ$_{surf}$ of the exposed surfaces, at the morphology, to achieve the complete map of morphologies for the cubic structure.

Morphology	A	B	C	D	E	F	G	H	I	J
$\gamma_{surf}^{(001)}/\gamma_{surf}^{(11x)}$					(001)					
(110)	1	0.5	2	1	1	0.5	2	0.4	1.25	2.13
(111)	1	0.5	1	2	0.5	1	2	0.8	1.25	2.5

This type of analysis is useful to gain further understanding of how to achieve morphological control of complex three-dimensional crystals by tuning the ratio of the values of γ$_{surf}$ of the different surfaces. As reported in several works in the literature [54-85], theoretical surface calculations associated with Wulff's construction are a powerful tool to modulate the possible morphologies of (nano/micro) materials. **Table 2** shows several published papers found in the literature that use our methodology [53] to match the theoretical and experimental morphologies.

Table 2. Materials studied using our theoretical approach.

| Material	Crystalline phase	Studies	Ref.
Ag	Cubic	Predict morphologies*	[53]
TiO_2	Anatase	Predict morphologies*	[53]
α-Fe_2O_3	Trigonal	Predict morphologies*	[47]
ZnS	Wurtzite	Optical properties and photocatalytic activity	[65]
In_2O_3	Cubic	Phase transition and electrocatalytic activity	[70]
		Predict morphologies*	[47]
Cu_2O	Cubic	Predict morphologies and calculate the possible paths of the morphological changes*	[74]
ZnO	Wurtzite	Photocatalytic activity	[75]
Co_3O_4	Cubic spinel	Predict morphologies*	[47]
Ag_2O	Cubic	Photocatalytic activity	[60]
$BaZrO_3$	Cubic	Predict morphologies*	[53]
t-$LaVO_4$	Tetragonal	Predict morphologies*	[57]
$BaMoO_4$	Tetragonal	Structural analysis and morphological transformation	[59]
$Ag_4V_2O_7$	Orthorhombic	Electronic structure and optical properties	[62]
$CuMnO_2$	Monoclinic	Electronic structure and magnetism	[63]
Ag_3PO_4	Cubic	Photoluminescence and photocatalytic properties	[58]
$CaMoO_4$	Tetragonal	Photoluminescence emission	[66]
β-$ZnMoO_4$	Monoclinic	Investigation of the surfaces and morphologies*	[67]
$MnTiO_3$	Trigonal	Magnetism and multiferroic properties*	[71]
$BiPO_4$	Hexagonal and Monoclinic	Morphological, structural, electronic, and optical properties	[73]
α-Ag_2WO_4	Orthorhombic	Predict morphologies*	[53]
		Antibacterial and photocatalytic activity	[77]
		Photocatalytic activity	[86]
β-Ag_2MoO_4	Cubic spinel	Antifungal activity and photoluminescence emission	[79]
		Antibacterial activity	[87]
$PbNiO_3$	Trigonal	Predict morphologies and associated the properties with the exposed surfaces with different number of oxygen vacancies*	[81]
Ag_2CrO_4:Zn^{2+}	Orthorhombic	Photoluminescence emission, antibacterial and photocatalytic activity	[85]
γ-Ag_2WO_4	Cubic	Photoluminescence emission	[83]

*Only theoretical investigation

2.3. How to trace the energy profiles connecting the different morphologies

The path that connects the different morphologies depends on the ratio between the values of γ_{surf} of the exposed surfaces in the crystal morphology. During the synthesis of the materials, all the surfaces suffer a process of stabilization or destabilization. If a given surface is energetically favored along the growth process, this surface enhances their presence in the final morphology with a lower γ_{surf} value. In order to match the experimental and the theoretical morphology, we can trace the reaction pathway that displays the evolution of the morphologies. This strategy was proposed and employed with success by our research group [86] by calculating the polyhedron energy (E_{poly}). The E_{poly} is obtained by using the equation (2):

$$E_{poly} = \sum C_i \times \gamma_{surf}^{(hkl)} \tag{2}$$

where C_i is the percentage of contribution of the surface area ($A^{(hkl)}$) to the total area of polyhedron (A^{poly}), $C_i = A^{(hkl)}/A^{poly}$ and $\gamma_{surf}^{(hkl)}$ is the surface energy [86].

In **Fig. 4**, the energy profiles of the morphological transformations (from **A** to **E**, **F** and **H**, via **B**) are displayed. By decreasing the value of γ_{surf} for the (001) surface, the morphology **B** is reached. From this point three different pathways are possible: (i) by decreasing the value of γ_{surf} for the (110) surface, the morphology **E** is obtained; (ii) by decreasing the value of γ_{surf} for the (111) surface, the morphology **F** is obtained, and (iii) the last path achieves the morphology **H** by decreasing the value of γ_{surf} for the (001) and (111) surfaces. These channels are thermodynamically energetically favorable and they are barrierless processes. It is important to note that if this energy barrier cannot be determined, then it needs to be redefined, at the first stage, by quantum mechanical analysis as it tries to move through randomly changing atomic environments. In a second step, spin interactions will be considered for a better understanding of the surface reaction kinetics.
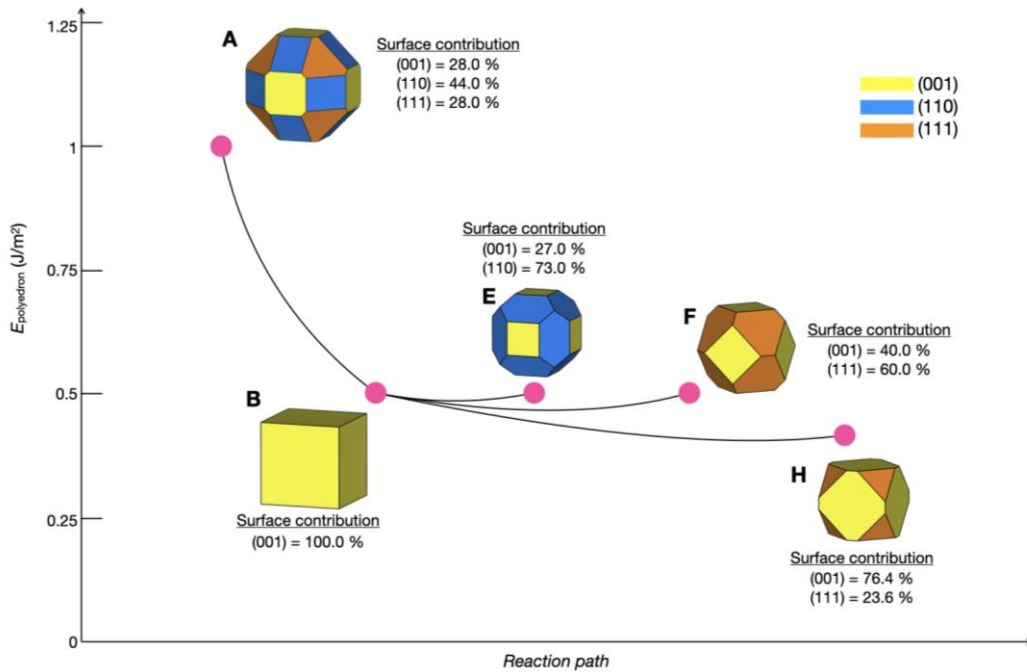
Fig. 4. A schematic representation of the energy profiles to obtain the morphology **E**, **F** and **H** from the morphology **A**, passing through the morphology **B**.

Although transition paths and thermodynamic aspects are now computationally feasible to simulate, as displayed in **Fig. 4**, a proposed mechanism and its corresponding energy profile are only one part within the kinetics realm of the transformation. In addition, a precise account of different reaction conditions, such as pressure and temperature also needs a kinetic model involving the variable time. Other kinetic phenomena that are difficult to modelize are due to, for example, the non-equivalent transformations of single crystal and powder samples or even to the coexistence of more than one morphology. This situation can lead to the appearance of different morphologies depending on the time scale of the experiment where the sample is kept. For all these reasons, phenomenological models and/or theoretical insights revealing when a morphology might emerge are always very valuable to guide temperature/pressure-based experiments and for an overall comprehension of the morphological sequence.

3. Surface composition: what really is important?

The surface properties of a crystal are crucial for understanding and designing new materials for many applications. In a simple way, defects can be generated by introducing or removing atoms onto or from the surface, and this modifies the coordination and energy of atoms at the exposed surfaces. In the last decade, atomically supplied nanomaterials with different sizes and exposed surfaces are excellent models for promoting catalytic studies. For example, technologies such as fuel cells and the manufacture of industrial chemicals use catalysts to accelerate transformations, which is fundamentally process-oriented by the surface of the material [3, 4, 88, 89].

The surface stability is described by the value of its γ_{surf}, a measure of the excess energy of atoms on the surface due to a variety of factors, such as broken bonds that result in atoms with a lower coordination number than those present in the bulk. This fundamental amount of energy is important to understand the surface structure, reconstruction, rugosity and the equilibrium morphology of the crystal. Despite its importance, the experimental determination of values of γ_{surf}, especially for specific surfaces, is difficult and rare [36-40].

The atoms in the bulk structure are surrounded by a specific number of atoms. In the case of β-Ag_2MoO_4, for example, the Ag atoms present a coordination number of 6 oxygen atoms, while the Mo atoms are surrounded by 4 oxygen atoms, which results in the octahedral $[AgO_6]$ and tetrahedral $[MoO_4]$ clusters, respectively, in the bulk structure, as illustrated in **Fig. 5**. These clusters are responsible for the formation of the cubic β-Ag_2MoO_4 structure. While in the bulk the atoms have the total atom coordination in the clusters, in the surfaces, the clusters present undercoordinated atoms, with distortion and oxygen vacancies due to the broken bonds. These undercoordinated clusters are responsible for the properties of the material and determine if the

material will present a high or low activity, as illustrated in **Fig. 1**. **Fig. 5** shows the clusters of the bulk and in the (001), (101) and (111) surfaces for the cubic β-Ag_2MoO_4 structure.
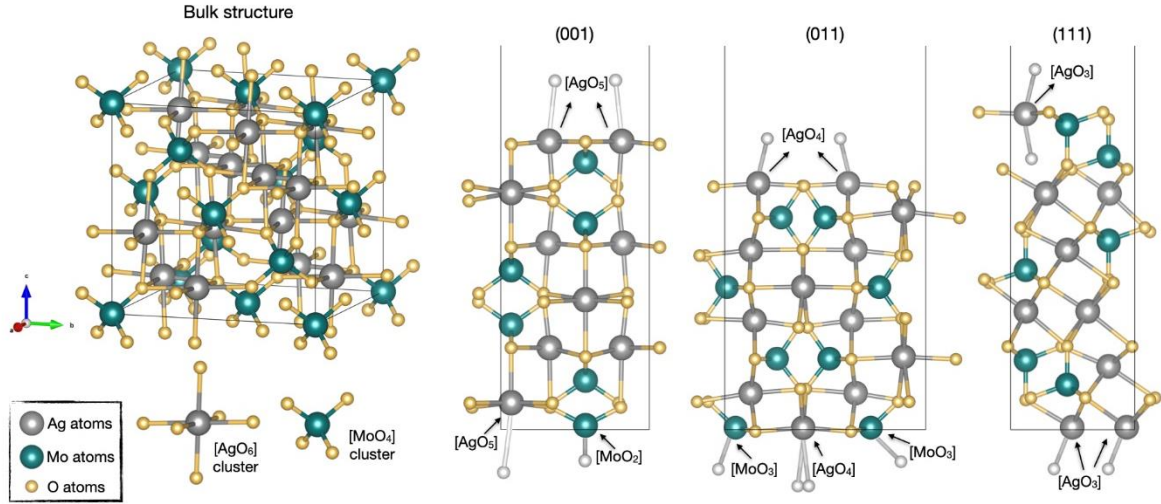
Fig. 5. Bulk and surfaces models for the cubic β-Ag_2MoO_4 structure. The Ag and Mo clusters on the bulk and in the surfaces are shown.

An analysis of **Fig. 5** renders that all surfaces present undercoordinated clusters where the dangling bonds were colored white. There are many kinds of clusters with one ($[AgO_5]$ and $[MoO_3]$ clusters), two ($[AgO_4]$ and $[MoO_2]$ clusters), and three ($[AgO_3]$ clusters) oxygen broken bonds for (001), (011) and (111) surfaces, respectively. These oxygen broken bonds can be interpreted as oxygen vacancies and written using the Kröger-Vink notation [90].These oxygen vacancies can have different electronic densities, represented by neutral vacancy, vacancy with one hole, or with two holes positive charges, forming a *n*-type semiconductor. On the other hand, they can have metal vacancies, with negative charge, being a semiconductor of *p*-type.

3.1. Kröger-Vink notation for exposed surfaces

Because of its fundamental ability to accommodate a large number of defects without destabilizing the crystal structure, semiconductors have become a technologically important

15

material that finds its use in many areas. These defects can be: vacancies, interstitial atom, substitutional atom, and impurity. The structural and electronic order-disorder degree of a metal oxide semiconductor is affected by the presence of many kinds of defects. Sometimes, depending on the type of defect (oxygen and/or metal vacancies), they may change their properties without the need for dopants; while the doping of semiconductors with acceptors and donors is essential for electronic and optoelectronic applications, having an important impact on the materials properties.

To better understand morphology and surface termination, we used the Kröger-Vink notation [90] to classify different types of clusters. The Kröger-Vink notation describes a defect **A** with effective charge **b** occupying a crystalline site **a** (A_a^b). When the defect is a vacancy the representation is V_a^b. The atomic clusters with undercoordinated atoms presented in the last layer of the surface can be written by the presence of neutral oxygen vacancies (V_o^x), where the sub index x means "neutral" in the Kröger-Vink notation [90]. Therefore, the undercoordinated clusters at the cubic β-Ag$_2$MoO$_4$ surfaces shown in **Fig. 5** can be rewritten with the presence of V_o^x, as illustrated in **Fig. 6**.
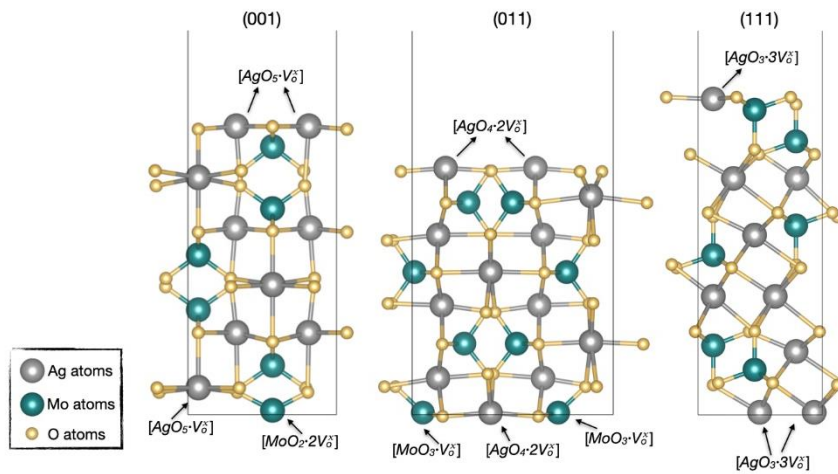
Fig. 6. Surfaces models for the cubic β-Ag$_2$MoO$_4$ structure with the undercoordinated clusters described by the Kröger-Vink notation.

In this way, the analysis of **Fig. 6**, results in the undercoordinated clusters at the surfaces: $[AgO_5 \cdot V_o^x]$ and $[MoO_3 \cdot V_o^x]$, $[AgO_4 \cdot 2V_o^x]$ and $[MoO_2 \cdot 2V_o^x]$ and $[AgO_3 \cdot 3V_o^x]$ for one, two, and three oxygen broken bonds, respectively. Based on this notation the mechanism to explain the semiconductor properties, like the photocatalysis, can be proposed. The kind of clusters that can be present in the materials structure is presented in **Table 3**. The clusters can display neutral charge (x), the positive charge, denoted by dots ($\bullet$), and the negative charge, represented by slashes ($'$) [91].

Table 3. Representation of the clusters with different kind of clusters using the Kröger-Vink notation.

Type of cluster	Meaning
$[MO_{z-y} \cdot yV_o^x]$	Metal cluster with "y" neutral oxygen vacancy
$[MO_{z-y} \cdot yV_o^{\bullet}]$	Metal cluster with "y" positive oxygen vacancy
$[MO_{z-y} \cdot yV_o^{\bullet\bullet}]$	Metal cluster with "y" double positive oxygen vacancy
$[MO_z]'$	Metal cluster charged negatively
$[MO_z]^{\bullet}$	Metal cluster charged positively
$[MO_z]^x$	Metal cluster with neutral charge

The precise prediction of the crystal morphology helps to save time and avoid technical trouble shoots of systems involved in the photocatalytic processes. Therefore, their rationalization, by exploring the chemical entities of the material emerging from a different crystal cleaved, helps to improve the applicability and efficiency of a given material. In the following, we will demonstrate that a systematic study of the different coordination of the atoms in the exposed surfaces in the morphologies of the materials allows us to explain their activities (photocatalytic and biocide). The precise control of these active sites and undercoordinated metal clusters with V_o^x in the exposed surfaces represented one fundamental step to the rational design of materials and provide a new way to think that can be extrapolated to a wide range of semiconductors.

3.2. Photocatalytic activity

The photocatalytic process occurs in three crucial steps: (1) harvesting light to produce e^-/h^+ pairs, (2) charge separation and migration from bulk to the exposed surface, and (3) the surface-reached charges trigger interfacial redox reactions at the corresponding active sites. To boost the photocatalytic behavior, it is fundamental to consider crystal surface exposure as an effective strategy to boost light absorption, charge separation, and interfacial redox reactions.

In order to investigate the influence of the morphology of the α-Ag₂WO₄ crystal on the photocatalytic activity, our research group [86] synthesized this material by the co-precipitation method. The results render that a hexagonal rod-like morphology is obtained, while the presence of the anionic surfactant sodium dodecyl sulfate (SDS), a cuboid-like morphology is reached [86]. The cuboid-like morphology presented a low photocatalytic activity towards the degradation of Rhodamine B (RhB) dye under UV light with respect to the hexagonal rod-like morphology. A detailed analysis of the geometry and electronic properties of the exposed surfaces at the morphology allowed us to explain and rationalize these results. In particular, the specific set of atoms with different kinds of arrangement, i.e., clusters with broken metal-oxygen bonds, and the presence of V_o^x.

As displayed in **Fig. 7**, the hexagonal rod-like morphology is composed of (001), (010) and (101) surfaces, the (101) surface being 50.0% of the morphology, while the cuboid-like morphology is composed of (001), (010) and (100) where these three surfaces represent 33.3% each. The adsorption of the SDS anionic head on the (100) surface provokes its stabilization and prevents the growth process along the (101) surface, giving rise to the cuboid-like morphology. Analysis of the type of clusters in each surface, suggests that the distorted $[WO_6]_d$ clusters are present in all surfaces along with undercoordinated clusters of Ag and W atoms. In the (101) surface, there are the undercoordinated $[AgO_4 \cdot 3V_o^x]$, $[AgO_5 \cdot 2V_o^x]$ and $[WO_5 \cdot V_o^x]$ clusters. The (001) surface is formed by the undercoordinated $[AgO_5 \cdot 2V_o^x]$,$[AgO_4 \cdot 3V_o^x]$,

$[AgO_4 \cdot 2V_o^x]$, and $[WO_5 \cdot V_o^x]$ clusters, while only the undercoordinated $[AgO_5 \cdot 2V_o^x]$ and the distorted $[AgO_4]_d$ clusters are present in the (010) surface. In the (100) surface from the cuboid-like morphology the undercoordinated $[AgO_5 \cdot 2V_o^x]$ and $[WO_4 \cdot 2V_o^x]$ clusters are present. For the α-Ag₂WO₄ crystals, the main reason for the superior photocatalytic activity is due to the presence of the (101) surface [86].
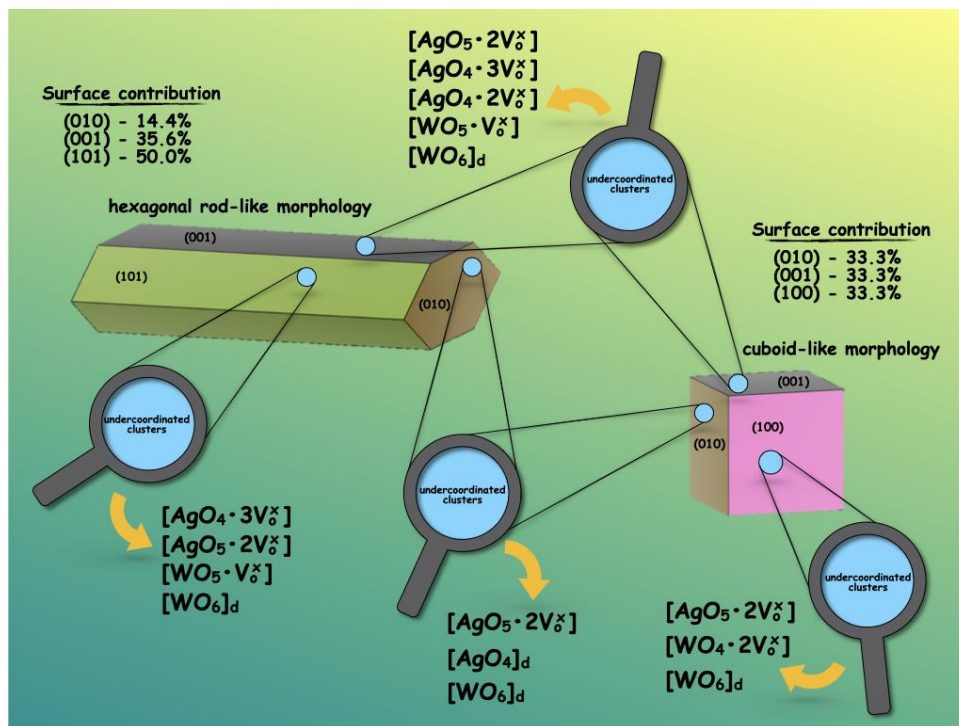
Fig. 7. Hexagonal rod- and cuboid-like morphologies of the α-Ag₂WO₄ crystals obtained by our research group [86].

The energy absorbed by the photocatalyst comprises the range of ultraviolet and/or visible light, even natural sunlight. When the photocatalyst absorbs light, if the energy of the photons is enough to excite the electrons in the valence band (VB), then they migrate to a higher energy level in the conduction band (CB) of the material. This phenomenon generates the charge carriers known as e^-/h^+ pairs.

Activations of molecular oxygen (O₂) and water (H₂O) is one of the most important chemical processes of immense interest and practical importance. These processes are
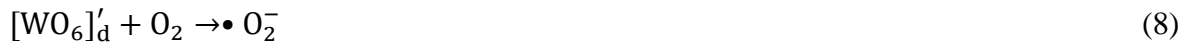
proceeded by electron transfer processes along redox reactions and conversion of nonreactive neutral atomic and molecular species in reactive triplet, doublet and singlets. The sensitiveness of a chemical reaction to spin would lead to an additional manipulation channel as the reaction product will not only depend on the total charge but may also depend on the spin of the electrons entering the chemical reaction. In a semiconductor, the photogenerated hole at the VB can migrate to the surface of the material and react with H_2O molecules to produce hydroxyl radicals ($\bullet OH$), while the photoexcited electron in the CB can react with the adsorbed molecular O_2 to produce superoxide radical ($\bullet O_2^-$). These photogenerated species are called reactive oxygen species (ROS). The researchers expressed the created ROS by chemical equations which are as follows:

$$Semiconductor + h\nu \longrightarrow e^- + h^+ \tag{3}$$

$$h^+ + H_2O \longrightarrow \bullet OH + H^+ \tag{4}$$

$$e^- + O_2 \longrightarrow \bullet O_2^- \tag{5}$$

The ROS are the key signaling molecules in both photocatalytic and physiological processes and play an important role in the development and function of photocatalytic and biocide materials. DFT calculations revealed that p-type and n-type conductivity can be ascribed to shallow acceptors (metal vacancies) and shallow donors (oxygen vacancies), respectively. Furthermore, these electronic states are located in the forbidden gap to undergo an ionization process to form electronic defects, i.e., quasi-free e^- and h^+ [92, 93]. Furthermore, it was demonstrated that the recombination of e^-/h^+ pairs is probable at bulk sites while surface defects improve the reactivity by promoting the adsorption of O_2 and H_2O. Then, exposed surfaces with a difference in charge density (due to the dipole moment) bind the adsorbates strongly and drive the photocatalytic reactions [94-96]. The ability to control these properties at the nanoscale has allowed correlations to be made between nanocrystal structure and their optical, magnetic, and electronic properties, which has implicated these materials in various

applications ranging from biomarkers to photocatalysts. The rational pathway between crystal morphology and arrangement of atoms in crystal lattice opens the future of morphology-selective synthesis.

The generation of the e^-/h^+ pairs involves the cluster-to-cluster charge transfer process. At the exposed surface, these electronic rearrangements occurred from the $[AgO_y \cdot nV_o^x]$ and $[WO_z \cdot nV_o^x]$ clusters to $[WO_6]_d$, forming a negatively charged $[WO_6]_d'$ cluster and a positively charged $[AgO_y \cdot nV_o^\bullet]$ and $[WO_z \cdot nV_o^\bullet]$ clusters. Therefore, these clusters are the source of e^-/h^+, where the sub index "y" and "z" correspond to the number of coordination and "n" refers to the number of vacancies. Based on the analysis of these clusters, a mechanism is proposed to explain the formation of the ROS from H_2O and O_2 and the subsequent photocatalytic activity of α-Ag$_2$WO$_4$, as presented in the following equations:

$$[AgO_y \cdot nV_o^x] + [WO_6]_d \rightarrow [AgO_y \cdot nV_o^\bullet] + [WO_6]_d' \tag{6}$$

$$[WO_z \cdot nV_o^x] + [WO_6]_d \rightarrow [WO_z \cdot nV_o^\bullet] + [WO_6]_d' \tag{7}$$

$$[WO_6]_d' + O_2 \rightarrow \bullet\, O_2^- \tag{8}$$

$$[AgO_y \cdot nV_o^\bullet] + H_2O \rightarrow H^+ + \bullet\, OH \tag{9}$$

$$[WO_z \cdot nV_o^\bullet] + H_2O \rightarrow H^+ + \bullet\, OH \tag{10}$$

It is important to note that the band gap value is a key parameter controlling the photocatalytic activity of a given semiconductor. That value is quite dependent on the calculation methods, and specifically within DFT framework, from the exchange-correlation functional used [97-99]. However, the results of present study, based on the analysis of the morphology, are independent from the values of both bulk and surface band gaps.


3.3. Biocide activity

Semiconductors are an interesting class of materials for the fight against biocide infections as they can produce microorganism-killing radicals to prevent their transmission. It is well

known that ROS-generated material agents can be regarded as potential biocide agents because of the rapid oxidation of various biomacromolecules in cells. Although a low level of ROS has a significant effect on supporting the cellular life cycle, excessive ROS could generate oxidative stress, giving rise to oxidative damage to the cellular constituents (e.g., nucleotides). Through this property, ROS act as strong oxidants to destroy microorganisms and contribute to sterilization.

The influence of the morphological changes in the antibacterial activity was investigated for the β-Ag_2MoO_4 crystals by our research group [87]. The β-Ag_2MoO_4 crystals with different morphologies were obtained by a simple co-precipitation method using three different solvents: water, ammonia and ethanol. The antibacterial efficiency was tested against the methicillin-resistant *Staphylococcus aureus* (MRSA) and *Escherichia coli* (*E. coli*) and was observed that the efficacy for both bacteria increased according to the following order: water < ammonia < ethanol. A joint experimental and theoretical approach was employed to connect the morphology with biocide activity of the β-Ag_2MoO_4 crystals.
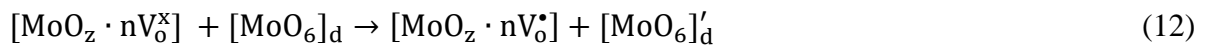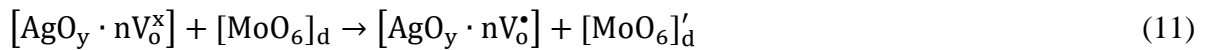
From the first-principles calculations of the values of γ_{surf} using the Wulff construction it was possible to modulate the experimental morphologies and correlate to the biocide activity.

Fig. 8 illustrates the undercoordinated clusters present in the (001), (011) and (111) surfaces of the β-Ag_2MoO_4 morphology.
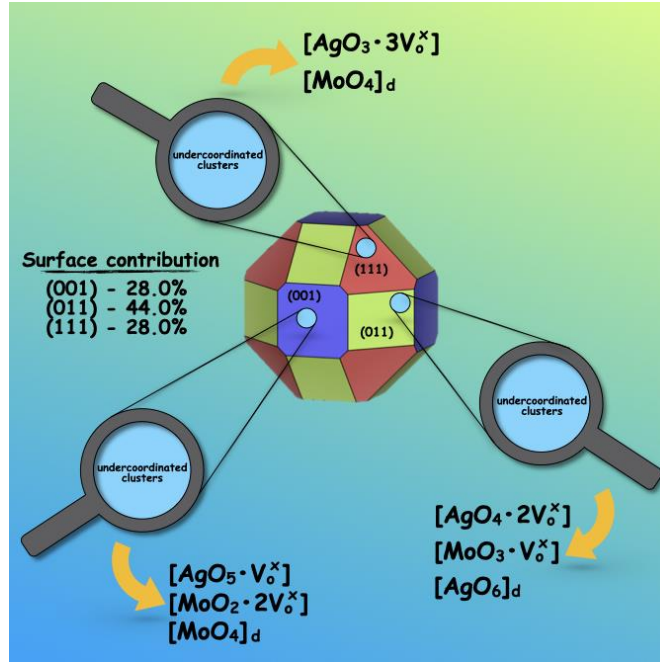
Fig. 8. Morphology of the β-Ag₂MoO₄ crystals obtained by our research group [87].

The β-Ag₂MoO₄ morphology is composed of the (011) surface with 44.0% of contribution and this surface is composed of $[AgO_4 \cdot 2V_o^x]$, $[MoO_3 \cdot V_o^x]$ and $[AgO_6]_d$ clusters. The (111) surface presents the $[AgO_3 \cdot 3V_o^x]$ and $[MoO_4]_d$ clusters, while the (001) surface is composed of $[AgO_5 \cdot V_o^x]$, $[MoO_2 \cdot 2V_o^x]$ and $[MoO_4]_d$ clusters, each one representing 28.0% of the morphology. Therefore, the undercoordinated $[AgO_y \cdot nV_o^\bullet]$ and $[MoO_z \cdot nV_o^\bullet]$ clusters will be the source of h^+ and the charged $[MoO_4]_d'$ clusters are the source of e^-, after the cluster-to-cluster charge transfer process. Therefore, the following mechanism is proposed for the generation of ROS associated to the biocide activity of β-Ag₂MoO₄:

$$[AgO_y \cdot nV_o^x] + [MoO_6]_d \rightarrow [AgO_y \cdot nV_o^\bullet] + [MoO_6]_d' \tag{11}$$

$$[MoO_z \cdot nV_o^x] + [MoO_6]_d \rightarrow [MoO_z \cdot nV_o^\bullet] + [MoO_6]_d' \tag{12}$$

$$[MoO_6]_d' + O_2 \rightarrow \bullet O_2^- \tag{13}$$

$$[AgO_y \cdot nV_o^\bullet] + H_2O \rightarrow H^+ + \bullet OH \tag{14}$$

$$[MoO_z \cdot nV_o^\bullet] + H_2O \rightarrow H^+ + \bullet OH \tag{15}$$

Considering the close relation between photocatalytic and biocide properties of semiconductors, their activity can be exerted though similar mechanisms. The corresponding activities are associated to the generation of ROS such as hydroxyl radical (•OH), superoxide radical (•O_2^-), singlet oxygen ($^1O_2$). These radicals formed via the trapping of photogenerated e^- and h^+, are widely considered as key players [100]. Other species such as hydrogen peroxide (H_2O_2), which is developed during the disproportionation of •O_2^- which transform to •OH and $^1O_2$, participate as oxidant agent. At nanoscale, both the surface atoms and structural defects increase, the active sites at the exposed surfaces exponentially increase to be able to churn out a plethora of ROS and provoke oxidative stress. A mechanism involving the generation of ROS by rationalizing the photocatalytic and biocide activities of α-Ag_2WO_4 and β-Ag_2MoO_4 materials, respectively, can be proposed, as illustrated in **Fig. 9**.
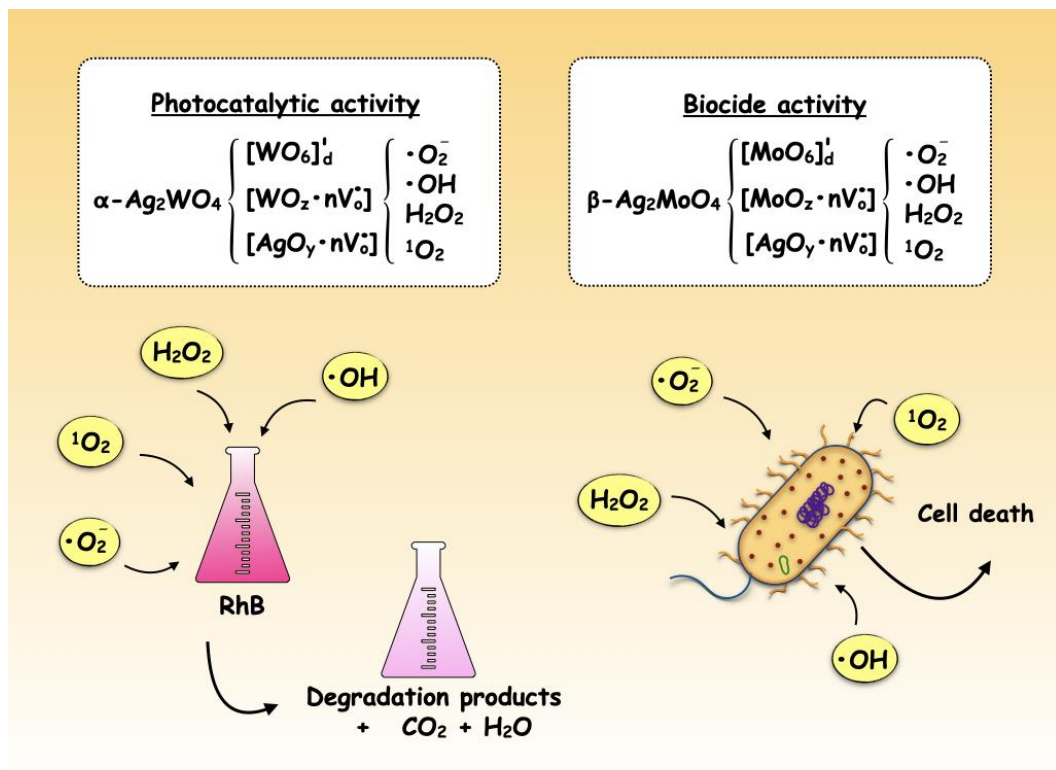
Fig. 9. A schematic representation of how α-Ag_2WO_4 and β-Ag_2MoO_4 semiconductors produce ROS, at the exposed surfaces of the morphology described by the Kröger-Vink notation. These ROS are responsible for the degradation process of RhB (photocatalytic activity) and the death of the cell membrane (biocide activity).

4. Conclusions

The chemical and physical properties of multifunctional semiconductor materials are susceptible to its morphology and surface chemistry. The active sites that are responsible for these properties are localized on the exposed surfaces, and, hence, surface-controlled synthesis of multi-dimensional materials via manipulating nucleation and growth for enhanced functionality has substantial importance. In this paper, we have discussed a new model for the prediction of crystal morphology, using Wulff construction and the values of γ_{surf} obtained by DFT calculations. The γ_{surf} represents the thermodynamic stability of a given surface and a lower γ_{surf} value indicates a more stable surface. According to the Wulff theorem, the equilibrium shapes of inorganic materials are obtained from their respective values of γ_{surf}. Therefore, with the γ_{surf} values calculated and associating with the Wulff construction it was possible to obtain the ideal morphology *in vacuum*.

The main objective is to analyze and disclose a general tool that can help the interpretation of the relationship between the morphology and activity (photocatalytic and biocide) of materials. The complete map of available morphology for many materials derived from first-principles calculations can be obtained, compared and matched with experimental FE-SEM images. Different materials were investigated to understand the morphology transformations as function of the different values of γ_{surf} of the exposed surfaces, since the structure and electronic properties change along the pathways connecting the morphologies. It has been established that the determination and application of the proposed method is easy and more accurate to predict the crystal morphology and can be applied to any material. In particular, we show how the presence of surface defects, i.e. undercoordinated clusters, induces different site and electronic distributions depending on different factors such as the density of defects and

the geometry. These distributions are analyzed for the α-Ag$_2$WO$_4$ and β-Ag$_2$MoO$_4$ complex ternary oxides to interpret the morphology and then are linked with their photocatalytic and biocide activity, respectively. The approach employed in the present project is successful in identifying low-energy structures and available morphologies, as largely verified by the DFT calculations. This is the first, necessary, step to link a complete surface structure and morphology analysis with the observed FE-SEM images, as well as to introduce the reasons for the generation of ROS at α-Ag$_2$WO$_4$ and β-Ag$_2$MoO$_4$ materials to explain the photocatalytic- and biocide-morphology dependent activity, respectively. This article provides a valuable and novel strategy to understand how ROS are generated in semiconductors with photoenhanced catalytic and biocide capability. Our goal is that the discussion from the present paper should help in understanding the results of the properties of multifunctional semiconductors by means of morphology. The power of combining experiments with simulation and theory is highlighted and this study could not have gone as far as it did without the constant back and forth between the experimental and theoretical results.

Acknowledgments

References

[1] M. Koper, Fuel Cell Catalysis: A Surface Science Approach, Wiley, New York, 2008.

[2] P. Ragesh, V.A. Ganesh, S.V. Naira, A.S. Nair, J. Mater. Chem. A, 2 (2014) 14773-14797.

[3] J.K. Norskov, T. Bligaard, J. Rossmeisl, C.H. Christensen, Nat. Chem., 1 (2009) 37-46.

[4] B. Hammer, J.K. Norskov, Theoretical surface science and catalysis - Calculations and concepts, in: B.C. Gates, H. Knozinger (Eds.) Advances in Catalysis, Vol 45: Impact of Surface Science on Catalysis, 2000, pp. 71-129.

[5] M.G. Taylor, N. Austin, C.E. Gounaris, G. Mpourmpakis, ACS Catal., 5 (2015) 6296-6301.

[6] Y.T. Luo, L. Tang, U. Khan, Q.M. Yu, H.M. Cheng, X.L. Zou, B.L. Liu, Nat. Commun., 10 (2019).

[7] M.A. Boles, D. Ling, T. Hyeon, D.V. Talapin, Nat. Mater., 15 (2016) 141-153.

[8] H. Tong, S.X. Ouyang, Y.P. Bi, N. Umezawa, M. Oshikiri, J.H. Ye, Adv. Mater., 24 (2012) 229-251.

[9] A. McLaren, T. Valdes-Solis, G. Li, S.C. Tsang, J. Am. Chem. Soc., 131 (2009) 12540-12541.

[10] X.Q. Gong, A. Selloni, M. Batzill, U. Diebold, Nat. Mater., 5 (2006) 665-670.

[11] S. Rehman, W.L. Yang, F. Liu, Y. Hong, T. Wang, Y.L. Hou, Inorg. Chem. Front., 2 (2015) 576-583.

[12] W. Wu, R. Hao, F. Liu, X.T. Su, Y.L. Hou, J. Mater. Chem. A, 1 (2013) 6888-6894.

[13] C.H. Wang, J. Shi, X.M. Cui, J. Zhang, C.H. Zhang, L.C. Wang, B.L. Lv, J. Catal., 345 (2017) 104-112.

[14] J.B. Lian, X.C. Duan, J.M. Ma, P. Peng, T.I. Kim, W.J. Zheng, ACS Nano, 3 (2009) 3749-3761.

[15] C.W. Li, Z.Y. Gao, Minerals Engineering, 128 (2018) 123-132.

[16] B. Ni, X. Wang, Adv. Sci., 2 (2015) 1500085.

[17] S.W. Cao, F. Tao, Y. Tang, Y.T. Li, J.G. Yu, Chem. Soc. Rev., 45 (2016) 4747-4765.

[18] R.B. Hammond, Modelling Route Map: From Molecule Through the Solution State to Crystals, in: K.J. Roberts, R. Docherty, R. Tamura (Eds.) Engineering Crystallography: from Molecule to Crystal to Functional Form, Springer Netherlands, Dordrecht, 2017, pp. 71-108.

[19] S. Perkowitz, Optical characterization of semiconductors: infrared, Raman, and photoluminescence spectroscopy, Elsevier, 2012.

[20] M.H. Huang, G. Naresh, H.S. Chen, Acs Appl. Mater. Interfaces, 10 (2018) 4-15.

[21] M.H. Huang, Small, 15 (2019) 1804726.

[22] M.S. Hsieh, H.J. Su, P.L. Hsieh, Y.W. Chiang, M.H. Huang, Acs Appl. Mater. Interfaces, 9 (2017) 39086-39093.

[23] P.L. Hsieh, G. Naresh, Y.S. Huang, C.W. Tsao, Y.J. Hsu, L.J. Chen, M.H. Huang, J. Phys. Chem. C, 123 (2019) 13664-13671.

[24] J.Y. Huang, M. Madasu, M.H. Huang, J. Phys. Chem. C, 122 (2018) 13027-13033.

[25] A. Dhakshinamoorthy, S. Navalon, M. Alvaro, H. Garcia, ChemSusChem, 5 (2012) 46-64.

[26] A.F. Smith, S.E. Skrabalak, J. Mater. Chem. C, 5 (2017) 3207-3215.

[27] C. Tan, C. Qin, B. Sadtler, J. Mater. Chem. C, 5 (2017) 5628-5642.

[28] A. Pescaglini, D. Iacopino, J. Mater. Chem. C, 3 (2015) 11785-11800.

[29] A. Dey, Mater. Sci. Eng. B, 229 (2018) 206-217.

[30] Z.Y. Hai, Z.H. Wei, C.Y. Xue, H.Y. Xud, F. Verpoort, J. Mater. Chem. C, 7 (2019) 12968-12990.

[31] V.M. Zhyrovetsky, D.I. Popovych, S.S. Savka, A.S. Serednytski, Nanoscale Res. Lett., 12 (2017) 132.

[32] Y. Liu, Y. Jiao, Z.L. Zhang, F.Y. Qu, A. Umar, X. Wu, ACS Appl. Mater. Interfaces, 6 (2014) 2174-2184.

[33] J.S. Chen, X.W. Lou, Small, 9 (2013) 1877-1893.

[34] A. Kar, S. Kundu, A. Patra, RSC Advances, 2 (2012) 4879-4885.

[35] S. Thoka, A.T. Lee, M.H. Huang, ACS Sustainable Chem. Eng., 7 (2019) 10467-10476.

[36] W.R. Tyson, W.A. Miller, Surf. Sci., 62 (1977) 267-276.

[37] J.J. Gilman, J. Appl. Phys., 31 (1960) 2208-2218.

[38] J.J. Metois, P. Muller, Surf. Sci., 548 (2004) 13-21.

[39] D.J. Eaglesham, A.E. White, L.C. Feldman, N. Moriya, D.C. Jacobson, Phys. Rev. Lett., 70 (1993) 1643-1646.

[40] C. Bombis, A. Emundts, M. Nowicki, H.P. Bonzel, Surf. Sci., 511 (2002) 83-96.

[41] P.L. Hansen, J.B. Wagner, S. Helveg, J.R. Rostrup-Nielsen, B.S. Clausen, H. Topsoe, Science, 295 (2002) 2053-2055.

[42] E. Ringe, R.P. Van Duyne, L.D. Marks, Nano Lett., 11 (2011) 3399-3403.

[43] G. Wulff, Z. Kristallogr., 34 (1901) 449-530.

[44] M. Chen, B.H. Wu, J. Yang, N.F. Zheng, Adv. Mater., 24 (2012) 862-879.

[45] H. Guo, A.S. Barnard, J. Mater. Chem., 21 (2011) 11566-11577.

[46] L.D. Marks, L. Peng, J. Phys.: Condens. Matter, 28 (2016) 053001.

[47] M.M. Ferrer, A.F. Gouveia, L. Gracia, E. Longo, J. Andres, Modell. Simul. Mater. Sci. Eng., 24 (2016) 025007-025016.

[48] F.Z. Jiang, L. Yang, D.L. Zhou, G. He, J.B. Zhou, F.H. Wang, Z.G. Chen, Appl. Surf. Sci., 436 (2018) 989-994.

[49] A.S. Barnard, P. Zapol, J. Chem. Phys., 121 (2004) 4276-4283.

[50] A.S. Barnard, L.A. Curtiss, Rev. Adv. Mater. Sci., 10 (2005) 105-109.

[51] P. Muller, C. Mottet, J. Comput. Theor. Nanosci., 4 (2007) 316-325.

[52] X.X. Tian, T. Wang, L.F. Fan, Y.K. Wang, H.G. Lu, Y.W. Mu, Appl. Surf. Sci., 427 (2018) 357-362.

[53] J. Andrés, L. Gracia, A.F. Gouveia, M.M. Ferrer, E. Longo, Nanotechnology 26 (2015) 405703-405713.

[54] R.A. Roca, P.S. Lemos, J. Andrés, E. Longo, Chem. Phys. Lett., 644 (2016) 68-72.

[55] P.F.S. Pereira, A.F. Gouveia, M. Assis, R.C. de Oliveira, I.M. Pinatti, M. Penha, R.F. Goncalves, L. Gracia, J. Andres, E. Longo, Phys. Chem. Chem. Phys., 20 (2018) 1923-1937.

[56] W.d.S. Pereira, J. Andres, L. Gracia, M.A. San-Miguel, E.Z. da Silva, E. Longo, V.M. Longo, Phys. Chem. Chem. Phys., 17 (2015) 5352-5359.

[57] A.F. Gouveia, M.M. Ferrer, J.R. Sambrano, J. Andres, E. Longo, Chem. Phys. Lett., 660 (2016) 87-92.

[58] G. Botelho, J. Andres, L. Gracia, L.S. Matos, E. Longo, ChemPlusChem, 81 (2016) 202-212.

[59] M.C. Oliveira, L. Gracia, I.C. Nogueira, M.F.C. Gurgel, J.M.R. Mercury, E. Longo, J. Andres, Cryst. Res. Technol., 51 (2016) 634-644.

[60] R.A.P. Ribeiro, M.C. Oliveira, M.R.D. Bomio, S.R. de Lazaro, J. Andres, E. Longo, Appl. Surf. Sci., 509 (2020).

[61] J. Meng, Z.Y. Lan, Q.Y. Lin, T. Chen, X. Chen, X. Wei, Y.H. Lu, J.X. Li, Z. Zhang, J Mater Sci, 54 (2019) 1967-1976.

[62] R.C. de Oliveira, L. Gracia, M. Assis, M.S. Li, J. Andres, E. Longo, L.S. Cavalcante, CrystEngComm, 18 (2016) 6483-6491.

[63] A.A.G. Santiago, R.L. Tranquilin, M.C. Oliveira, R.A.P. Ribeiro, S.R. de Lazaro, M.A. Correa, F. Bohn, E. Longo, F.V. Motta, M.R.D. Bomio, J. Phys. Chem. C, 124 (2020) 5378-5388.

[64] S.C.S. Lemos, F.C. Romeiro, L.F. de Paula, R.F. Goncalves, A.P. de Moura, M.M. Ferrer, E. Longo, A.O.T. Patrocinio, R.C. Lima, J. Solid State Chem., 249 (2017) 58-63.

[65] F.A. La Porta, A.E. Nogueira, L. Gracia, W.S. Pereira, G. Botelho, T.A. Mulinari, J. Andres, E. Longo, J. Phys. Chem. Solids, 103 (2017) 179-189.

[66] F.K.F. Oliveira, M.C. Oliveira, L. Gracia, R.L. Tranquilin, C.A. Paskocimas, F.V. Motta, E. Longo, J. Andres, M.R.D. Bomio, J. Phys. Chem. Solids, 114 (2018) 141-152.

[67] R.A.P. Ribeiro, M.C. Oliveira, A.G. de Sousa, M.R.D. Bomio, F.V. Motta, L. Gracia, S.R. de Lazaro, E. Longo, J. Andres, J. Appl. Phys., 126 (2019).

[68] R.A. Roca, A.F. Gouveia, P.S. Lemos, L. Gracia, J. Andres, E. Longo, Inorg. Chem., 55 (2016) 8661-8671.

[69] G. Byzynski, C. Melo, D.P. Volanti, M.M. Ferrer, A.F. Gouveia, C. Ribeiro, J. Andres, E. Longo, Mater. Des., 120 (2017) 363-375.

[70] S.C.S. Lemos, E. Nossol, J.L. Ferrari, E.O. Gomes, J. Andres, L. Gracia, I. Sorribes, R.C. Lima, Inorg. Chem., 58 (2019) 11738-11750.

[71] R.A.P. Ribeiro, J. Andres, E. Longo, S.R. Lazaro, Appl. Surf. Sci., 452 (2018) 463-472.

[72] R.C. de Oliveira, C.C. de Foggi, M.M. Teixeira, M.D.P. da Silva, M. Assis, E.M. Francisco, B. Pimentel, P.F.D. Pereira, C.E. Vergani, A.L. Machado, J. Andres, L. Gracia, E. Longo, ACS Appl. Mater. Interfaces, 9 (2017) 11472-11481.

[73] A.C.M. Tello, M. Assis, R. Menasce, A.F. Gouveia, V. Teodoro, N. Jacomaci, M.A. Zaghete, J. Andres, G.E. Marques, M.D. Teodoro, A.B.F. da Silva, J. Bettini, E. Longo, Inorg. Chem., 59 (2020) 7453-7468.

[74] M.M. Ferrer, G.S.L. Fabris, B.V. de Faria, J.B.L. Martins, M.L. Moreira, J.R. Sambrano, Heliyon, 5 (2019).

[75] A.C. Catto, M.M. Ferrer, O.F. Lopes, V.R. Mastelaro, J. Andres, L.F. da Silva, E. Longo, W. Avansi, Appl. Surf. Sci., 529 (2020).

[76] D.H.M. Azevedo, G.S.L. Fabris, J.R. Sambrano, J.M.M. Cordeiro, Comput. Mater. Sci., 171 (2020).

[77] L.O. Laier, M. Assis, C.C. Foggi, A.F. Gouveia, C.E. Vergani, L.C.L. Santana, L.S. Cavalcante, J. Andres, E. Longo, Theor. Chem. Acc., 139 (2020).

[78] M.C. Oliveira, L. Gracia, I.C. Nogueira, M.F.D. Gurgel, J.M.R. Mercury, E. Longo, J. Andres, Ceram. Int., 42 (2016) 10913-10921.

[79] M.T. Fabbro, C.C. Foggi, L.P.S. Santos, L. Gracia, A. Perrin, C. Perrin, C.E. Vergani, A.L. Machado, J. Andres, E. Cordoncillo, E. Longo, Dalton Trans., 45 (2016) 10736-10743.

[80] G.S. Silva, L. Gracia, M.T. Fabbro, L.P.S. dos Santos, H. Beltran-Mir, E. Cordoncillo, E. Longo, J. Andres, Inorg. Chem., 55 (2016) 8961-8970.

[81] L.H.D. Lacerda, S.R. de Lazaro, J Mater Sci, 55 (2020) 6875-6890.

[82] R.A.P. Ribeiro, L.H.S. Lacerda, E. Longo, J. Andres, S.R. de Lazaro, J. Magn. Magn. Mater., 475 (2019) 544-549.

[83] R.A. Roca, P.S. Lemos, L. Gracia, J. Andres, E. Longo, RSC Advances, 7 (2017) 5610-5620.

[84] R.L. Tranquilin, L.X. Lovisa, C.R.R. Almeida, C.A. Paskocimas, M.S. Li, M.C. Oliveira, L. Gracia, J. Andres, E. Longo, F.V. Motta, M.R.D. Bomio, J. Phys. Chem. C, 123 (2019) 18536-18550.

[85] I.M. Pinatti, A.C.M. Tello, A.B. Trench, C.C. de Foggi, P.F.S. Pereira, M.M. Teixeira, N. Jacomaci, J. Andres, E. Longo, J. Alloys Compd., 835 (2020).

[86] N.G. Macedo, A.F. Gouveia, R.A. Roca, M. Assis, L. Gracia, J. Andrés, E.R. Leite, E. Longo, J. Phys. Chem. C, 122 (2018) 8667-8679.

[87] C.C. De Foggi, R.C. De Oliveira, M. Assis, M.T. Fabbro, V.R. Mastelaro, C.E. Vergani, L. Gracia, J. Andrés, E. Longo, A.L. Machado, Mater. Sci. Eng.: C, (2020) 110765.

[88] J. Greeley, J.K. Norskov, M. Mavrikakis, Annu. Rev. Phys. Chem., 53 (2002) 319-348.

[89] V. Stamenkovic, B.S. Mun, K.J.J. Mayrhofer, P.N. Ross, N.M. Markovic, J. Rossmeisl, J. Greeley, J.K. Norskov, Angew. Chem. Int. Ed., 45 (2006) 2897-2901.

[90] F.A. Kröger, H.J. Vink, Solid State Phys., 3 (1956) 307-435.

[91] T. Norby, J. Korean Ceram. Soc., 47 (2010) 19-25.

[92] J. Xiong, J. Di, J.X. Xia, W.S. Zhu, H.M. Li, Adv. Funct. Mater., 28 (2018).

[93] J. Nowotny, M.A. Alim, T. Bak, M.A. Idris, M. Ionescu, K. Prince, M.Z. Sahdan, K. Sopian, M.A.M. Teridi, W. Sigmund, Chem. Soc. Rev., 44 (2015) 8424-8442.

[94] T. Hisatomi, K. Domen, Nat. Catal., 2 (2019) 387-399.

[95] B. Mei, K. Han, G.D. Mul, ACS Catal., 8 (2018) 9154-9164.

[96] K. Appavoo, M.Z. Liu, C.T. Black, M.Y. Sfeir, Nano Lett., 15 (2015) 1076-1082.

[97] E.J. Baerends, Phys. Chem. Chem. Phys., 19 (2017) 15639-15656.

[98] E.J. Baerends, J. Chem. Phys., 149 (2018).

[99] A. Morales-Garcia, R. Valero, F. Illas, J. Phys. Chem. C, 121 (2017) 18862-18866.

[100] Y. Nosaka, A.Y. Nosaka, Chem. Rev., 117 (2017) 11302-11336.